Nano Research

Open Access

Research Article

Quantitative incorporation of dopants in medium-entropy cathodes for sodium-ion batteries: From design to validation

Chao Zhang[1,2], Huihui Zhao[2], Ning Fu[2], Jiacheng Fan[1], Bowen Zhang[1], Wenlei Jia[1], Pengtao Wang[1], Kun Xie[3], and Long Lin[1] ✉

[1] School of Materials Science and Engineering, Henan Polytechnic University, Jiaozuo 454003, China
[2] School of Materials Science and Engineering, Anyang Institute of Technology, Anyang 455000, China
[3] School of Cable Engineering, Henan Institute of Technology, Xinxiang 453003, China

Cite this article: *Nano Research*, **2026**, *19*, 94908572. https://doi.org/10.26599/NR.2026.94908572

ABSTRACT: The diffusion kinetics of electrons and ions are enhanced by the beneficial medium-entropy effect in medium-entropy cathodes, which results in a significant improvement of sodium storage capacity. However, the design of medium-entropy materials is usually characterized by high randomness and uncertainty, primarily due to the absence of established quantitative design methodologies. In this paper, $NaMn_{4/12}Fe_{3/12}Ni_{4/12}Ti_{1/12}O_2$ (MFNT), a medium-entropy (1.286 R) cathode material for sodium-ion batteries, was rationally designed based on a quantitative doping threshold determined via theoretical screening. The distinct contributions of Ni, Fe, and Ti to enhancing redox potential, improving electrical conductivity, modulating redox activity of transition metals (TM), inhibiting phase transitions, and enabling oxygen charge compensation were investigated systematically. Featuring a medium-entropy crystalline state, MFNT delivered a specific capacity of 127 $mAh \cdot g^{-1}$ at 0.1 C. After 100 cycles, 96 $mAh \cdot g^{-1}$ was retained, and even at 5 C, 71 $mAh \cdot g^{-1}$ was sustained. The entropy-stabilized structure, activated oxygen redox, and enhanced Na^+ diffusion kinetics were confirmed experimentally. The reversibility of phase transitions during the electrochemical reaction of this medium-entropy cathode was verified by *ex-situ* X-ray diffraction. The combined computational–experimental strategy accelerates material development and promotes sustainable design principles for next-generation sodium-ion batteries.

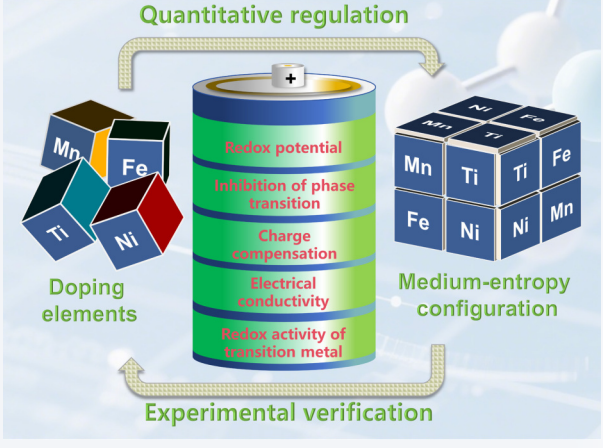

KEYWORDS: sodium-ion battery, quantitative design, multi-ion doping, first-principles calculation, medium-entropy

1 Introduction

Sodium-ion batteries (SIBs) are promising alternative to lithium-ion batteries (LIBs) due to the rich raw material reserves, wide distribution, and low cost [1]. Among various cathode materials, O3-type layered oxides are regarded as viable candidates for SIBs due to their high sodium-ion content and substantial theoretical reversible capacity [2–4]. However, the poor cycle and rate capability of O3-type layered oxides limit their large-scale application [5]. Previous studies have demonstrated that cation doping can enhance the performance of O3-type layered oxides by effectively regulating their phase ratios, triggering anionic redox reactions, and suppressing detrimental phase transitions [6]. To achieve a balance between performance, cost, and environmental impact, Mn, Fe, Ni, and Ti are commonly preferred as dopants in sodium-ion cathode materials. These elements are earth-abundant, low-cost, and environmentally benign compared to Co, Cr, or V, which are often used in LIB cathodes but suffer from toxicity, high price, and supply risks. Specifically, Ni is introduced to enhance voltage and capacity, and is considered less critical than Co in terms of resource scarcity [7–10]. Fe, being one of the most abundant metals on Earth, is employed to provide a low-cost and eco-friendly redox couple (Fe^{3+}/Fe^{4+}) [11, 12]. Ti is incorporated to suppress structural distortion, and is valued for its chemical stability, non-toxicity, and low cost [13].

Received: December 3, 2025; **Revised:** February 9, 2026
Accepted: February 13, 2026

✉Address correspondence to linlong@hpu.edu.cn

However, undesirable effects may also be induced by single-element doping, because a balance among all properties is required. For instance, the cycling reversibility can be enhanced by Ti doping, but at the same time leads to a decrease in specific capacity due to the closed-shell d-orbital configuration of Ti^{4+} [14, 15]. Therefore, a balanced co-doping approach is essential to optimize overall performance while maintaining economic viability and environmental compatibility. Meanwhile, the conformational entropy of the cathode material increases accordingly with the increase in the number of dopant elements. Owing to entropy stabilization, medium-entropy oxides (MEOs, 1.0–1.5 R) and high-entropy oxides (HEOs, ≥ 1.5 R) exhibit significantly enhanced electron and ion diffusion kinetics compared with low-entropy oxides (LEOs, ≤ 1.0 R), thereby substantially increasing the sodium storage capacity [16, 17]. Configurational entropy stabilization is maximized via co-doping of lattice-matching and physicochemically complementary elements at near-equimolar ratios; and functional threshold concentrations of each element are precisely tailored to preserve lattice integrity, balance redox activity and ion diffusion kinetics, and achieve synergistic optimization of capacity, rate capability, and cycling stability. Yao et al. [18] successfully synthesized a high-entropy $Na_{2/3}Li_{1/6}Fe_{1/6}Co_{1/6}Ni_{1/6}Mn_{1/3}O_2$ cathode, which demonstrated excellent electrochemical performance unaffected by phase transitions and oxygen redox reactions. High reversible capacity and long-term cycling stability were achieved. Mu et al. [19] explored $Na_{0.85}Li_{0.05}Ni_{0.25}Cu_{0.025}Mg_{0.025}Fe_{0.05}Al_{0.05}Mn_{0.5}Ti_{0.05}O_2$, which delivered a discharge capacity of 122 mAh·g^{-1} at 0.2 C and maintained 90% of its capacity after 1000 cycles at 10 C. Hong et al. [6] prepared a medium-entropy cathode material by introducing Fe, Mg, and Li into the traditional P2-type $Na_{0.75}Ni_{0.25}Mn_{0.75}O_2$ cathode. This material effectively mitigates the detrimental P2–O2 phase transition that occurs at high voltages. The cathode exhibits an exceptional rate performance, delivering a capacity of 108.4 mAh·g^{-1} at 10 C, with a capacity retention of 99.0% after 200 cycles at 1 C. Notably, configurations of all HEOs and MEOs reported in the literature are characterized by randomness and uncertainty, and lack a quantitative theoretical foundation for dopant content during material design. In addition, the experimental validation of the doping dosages for all MEOs to achieve configurations with balanced multifaceted performance is considered impractical.

In this study, a novel medium-entropy (1.286 R) O3-type cathode material, $NaMn_{4/12}Fe_{3/12}Ni_{4/12}Ti_{1/12}O_2$ (MFNT), was designed by quantitative incorporation of dopants and successfully synthesized, representing a green and efficient strategy for developing cathode materials. By optimizing cation composition and leveraging the entropy-stabilized structure, MFNT exhibits enhanced electron and ion diffusion kinetics, leading to improved sodium storage capacity, rate capability, and cycling stability compared to low-entropy counterparts. Specifically, it delivers a reversible capacity of 127 mAh·g^{-1} at 0.1 C and retains 71 mAh·g^{-1} at 5 C, with 96 mAh·g^{-1} remaining after 100 cycles. This method quantitatively predicts the doping threshold before any experiments, offering a sustainable pathway for the rational design of medium-entropy oxide cathodes in sodium-ion batteries.

2 Results and discussion

2.1 Quantitative theoretical calculations

A typical structural schematic of the O3-type oxide, together with various doping configurations, is presented in Fig. 1(a). The influence of doping elements on Mn–O bonds across different configurations was investigated. Due to the distinct interactions between Mn–O and TM–O, the adjacent Mn–O bond lengths were altered asymmetrically upon doping. In these cases, the structural difference between FeO_6 and MnO_6 octahedrons remains subtle due to the relatively similar Fe–O and Mn–O interactions. In comparison, the bonding disparities among Ni–O, Ti–O, and Mn–O are manifested in the elongation or contraction of Mn–O bonds within adjacent MnO_6 octahedra, which occurs along distinct directions near the doping sites. The mean squared error (MSE) in the bond lengths of Mn–O adjacent to the TMO_6 octahedra demonstrates that the introduction of Ni has the greatest effect on the lattice distortion of the O–TM–O layers of the cathode material.

Based on the formation energies at various desodiation concentrations, the structural evolution is depicted in the convex-hull phase diagram (Figs. S1(a)–S1(c) in the Electronic Supplementary Material (ESM)), expressed as Eq. (S1) in the ESM. The results show that a higher doped concentration decreases the thermal stability of the structure regardless of the dopant type. This is due to the fact that an elevated doped concentration may augment the configurational disorder. In accordance with the lowest energy structures, the calculated redox potentials are exhibited in Fig. 1(b), expressed as Eq. (S2) in the ESM. The voltage is observed to decrease with increasing Ti content, whereas the increase in Fe content enhances the voltage, although its effect is more limited compared to Ni. The operating voltage reaches 4.1 V at high Ni doping levels (y = 4) in the highly desodiated state (x = 8), indicating Ni's superior effectiveness as a voltage-enhancing dopant in cathode materials.

The Jahn–Teller (JT) effect associated with Mn^{3+} can induce irreversible phase transitions and structural disorder, consequently impairing the reversible capacity and cycling performance [20]. The crystal configurations of P- and O-type layered oxides can be characterized by the ratio of the interlayer distances, specifically $d_{(O–Na–O)}/d_{(O–TM–O)}$. A value of approximately 1.62 distinguishes P-type from O-type oxides [21]. The elevated ratio in P-type oxides stems from a localized electron distribution within the O–TM–O slabs, resulting in reduced repulsion between adjacent O–Na–O slabs and heightened repulsion between adjacent O–TM–O slabs [22]. Consequently, this ratio can serve as an indicator of the phase state of layered oxides across various sodium concentrations [15]. The effects of dopants on phase transition characteristics are illustrated in Fig. 1(c). The phase transition boundary (y = 1.62) is reached by the Fe-doped cathode material at a low desodiation state (x = 1–3). No enhancement is observed even at a high doping level (y = 4), suggesting that Fe exerts only a limited inhibitory effect on the phase transition. In contrast, phase transitions in Ti-doped cathodes occur at comparatively high desodiation concentrations (x = 3–5). Remarkable suppression is achieved even with a low Ti doping level (y = 1), indicating that excellent phase transition suppression can be attained with minimal Ti incorporation. The inhibitory effect of Ni lies between those of Fe and Ti, and a pronounced enhancement is observed with increasing Ni concentration. Thus, suppression of the O3–P3 phase transition can be markedly intensified by raising the Ni doping level.

Bader charge analysis was utilized to examine the influence of dopants on the charge-transfer behavior of O^{n-} during desodiation. As depicted in Fig. S2 in the ESM, the average Bader charge of O^{n-} in $NaMnO_2$ increases from −1.24 e to −1.04 e upon desodiation,

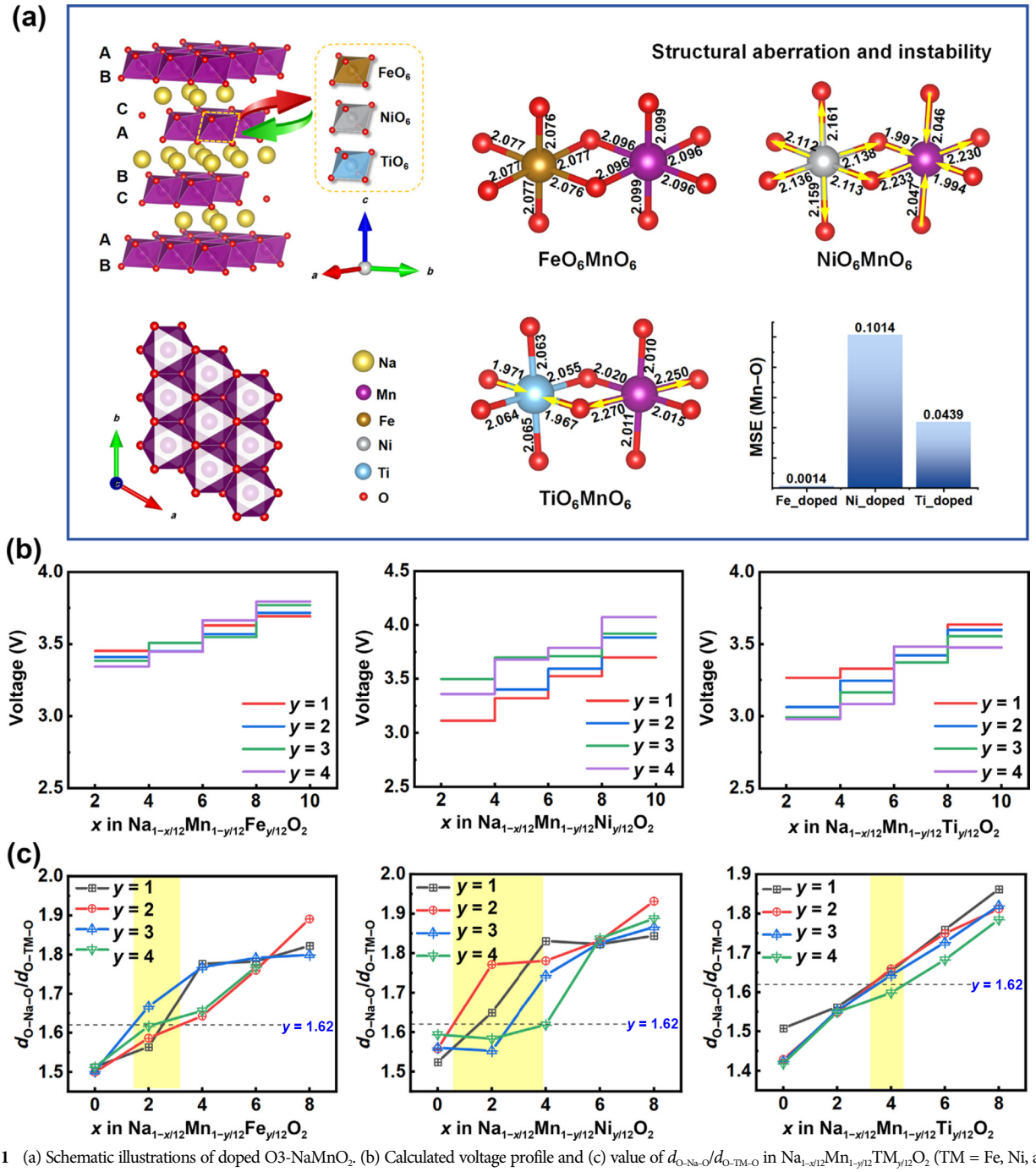

Figure 1 (a) Schematic illustrations of doped O3-$NaMnO_2$. (b) Calculated voltage profile and (c) value of $d_{O\text{-}Na\text{-}O}/d_{O\text{-}TM\text{-}O}$ in $Na_{1-x/12}Mn_{1-y/12}TM_{y/12}O_2$ (TM = Fe, Ni, and Ti, and $y = 1, 2, 3$, and 4).

demonstrating that O^{n-} acts as a redox center with a significant valence change. As shown in Fig. 2(a), the average Bader charge of O^{n-} in Fe-doped cathodes remains consistent with that of the intrinsic materials across all desodiation levels, indicating that Fe does not effectively facilitate charge compensation by O^{n-}. In contrast, a significant elevation in the average Bader charge is observed with increased Ni content, suggesting that the incorporation of Ni activates the redox activity and thereby enhances the reversible capacity of the electrode. Notably, contrary outcomes are observed upon the incorporation of Ti, with the average Bader charge decreasing as the Ti doping level increases. This suggests that Ti imposes an inhibitory influence on the charge compensation of O^{n-} during desodiation. Meanwhile, the redox activity of transition metals, recognized as the principal contributors to the capacity of SIBs, has been thoroughly investigated. The redox couples $Mn^{3+} \rightarrow Mn^{4+}$, $Fe^{3+} \rightarrow Fe^{4+}$, and $Ni^{2+} \rightarrow Ni^{3+} \rightarrow Ni^{4+}$ are respectively facilitated by Mn, Fe, and Ni through electron gain and loss in the d-orbitals. However, the closed-shell d-orbital configurations of Ti^{4+} are found to be incapable of contributing to the activity of the Ti^{4+}/Ti^{3+} redox couple, as displayed in Fig. 2(b). This conclusion will be further verified by the results of X-ray photoelectron spectroscopy (XPS).

The partial density of states (PDOS) of Mn 3d, Fe 3d, Ni 3d, Ti 3d, and O 2p were calculated and the results are shown in Fig. 2(c).

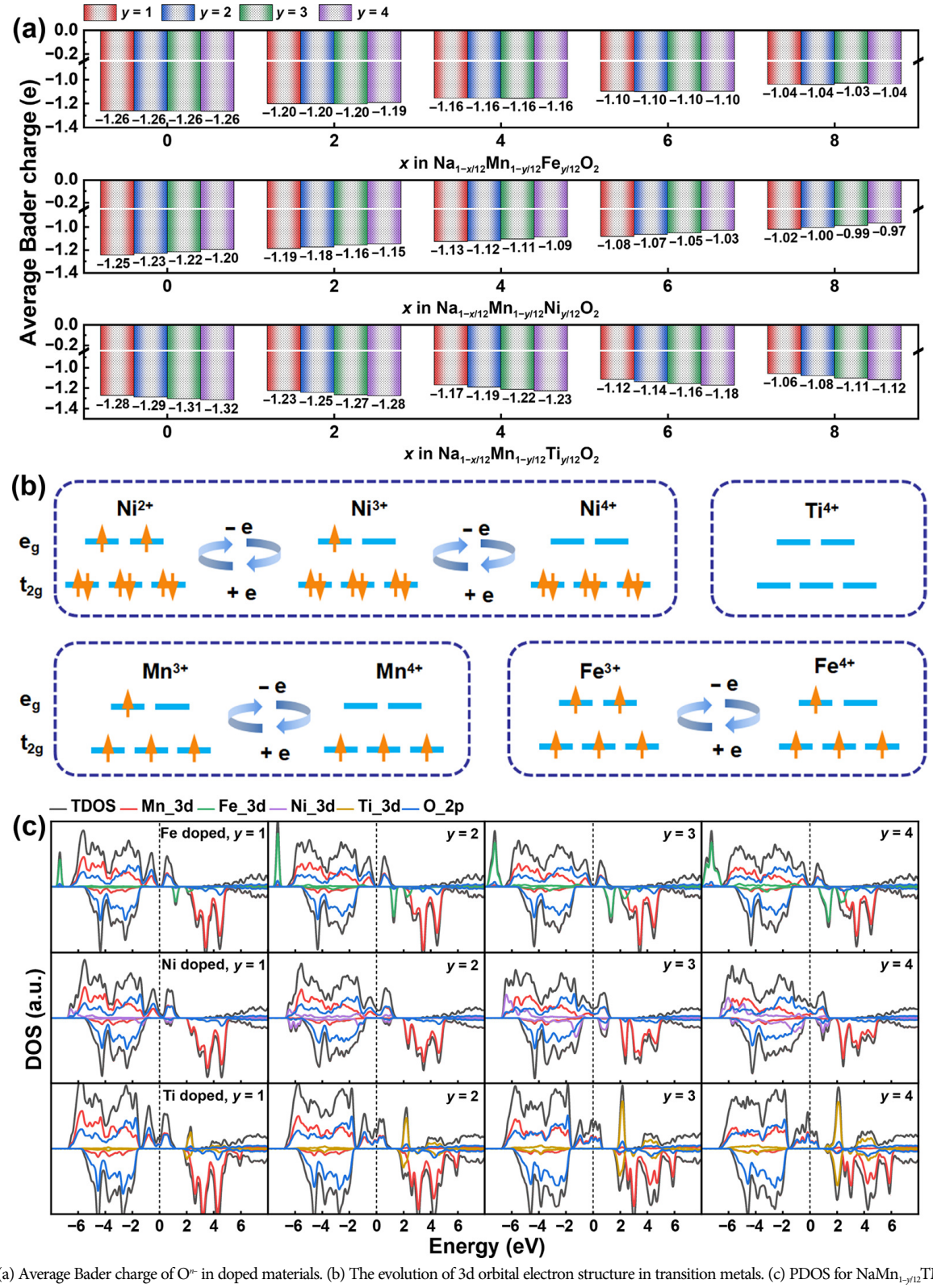

Figure 2 (a) Average Bader charge of O^{n-} in doped materials. (b) The evolution of 3d orbital electron structure in transition metals. (c) PDOS for $NaMn_{1-y/12}TM_{y/12}O_2$ (TM = Fe, Ni, and Ti, and y = 1, 2, 3, and 4).

All structures exhibit a distinct Mn 3d orbital distribution near the Fermi level (E_F), emphasising the crucial role of Mn^{3+} in redox activity. Additionally, significant overlap is observed between the Mn 3d and O 2p orbitals, signifying a robust d-p hybridization interaction between Mn and O [23]. At the E_F, the PDOS of Fe-doped cathodes is markedly lower than that of Ti- and Ni-doped counterparts, suggesting a reduced carrier density. This indicates that Fe incorporation is unlikely to significantly enhance intrinsic electronic conductivity. Intriguingly, a distinctive feature is observed at approximately −1 eV for Ni-doped cathodes: As the Ni

content increases, the PDOS of Mn 3d decrease, while that of O 2p exhibits a modest increase. This complementary variation indicates that Ni modifies the electronic structure of Mn^{3+}, thereby modulating the charge-compensation capabilities of both Mn 3d and O 2p orbitals [24]. Conversely, increased Ti content simultaneously attenuates the PDOS of Mn and O, suggesting a detrimental effect on the redox activity of Mn 3d and on the charge compensation ability of O 2p. Furthermore, as illustrated in Figs. S3 and S4 in the ESM, the intensified PDOS near the E_F upon desodiation suggest enhanced carrier density and, consequently, improved electronic conductivity [20].

Based on the analysis of properties such as redox potential, phase transition inhibition, O^{n-} charge compensation, transition metal redox activity, and electrical conductivity, a correlation between doping content and performance has been established, as presented in Table 1. As the doping content of Ni increases, the aforementioned properties are significantly enhanced. Although it has been demonstrated that Ti incorporation can effectively inhibit phase transitions, its contribution to increasing the redox potential and charge compensation capability remains limited. The introduction of Fe provides moderate improvements across multiple properties, and a higher Fe content can reduce material cost. In summary, we established the optimal medium-entropy configuration as MFNT, and thoroughly validated the diverse properties associated with this specific composition.

The crystal structure of MFNT is shown schematically in Fig. 3(a), which was obtained by screening the lowest energy configuration in Fig. S5 in the ESM. As shown in Fig. 3(b), the substantial negative formation energy of MFNT highlights its characteristic multi-electron reaction behaviour [20]. In accordance with the lowest energy structures, the calculated redox potential is exhibited in Fig. 3(c). Its excellent operating voltage of 4.12–4.33 V significantly exceeds the performance of $NaMn_{8/12}Ni_{4/12}O_2$ (NMNO). As can be seen in Fig. 3(d), the average Bader charge shifts from −1.24 e to −0.98 e. This phenomenon is unprecedented among all single-doped configurations and suggests that MFNT is proficient at providing additional capacity from O^{n-}. As depicted in Fig. 3(e), the phase transition characteristics of NFMT reveal that the Na^+ concentration at the phase transition boundary is comparable to that of $NaMn_{8/12}Ti_{4/12}O_2$ (NMTO), highlighting MFNT's remarkable ability to suppress the O3–P3 phase transition. Due to the entropy stabilization effect, the O3–P3 phase transition is rendered more

Table 1 The optimal doping content of dopants in different properties

Properties	Dopants		
	Fe	Ni	Ti
Redox potential	2/12–3/12	4/12	1/12
Inhibition of phase transition	2/12–3/12	4/12	1/12
Charge compensation of TM	2/12–3/12	4/12	1/12
Redox activity of O^{n-}	2/12–3/12	4/12	1/12
Electrical conductivity	2/12–3/12	4/12	2/12–3/12

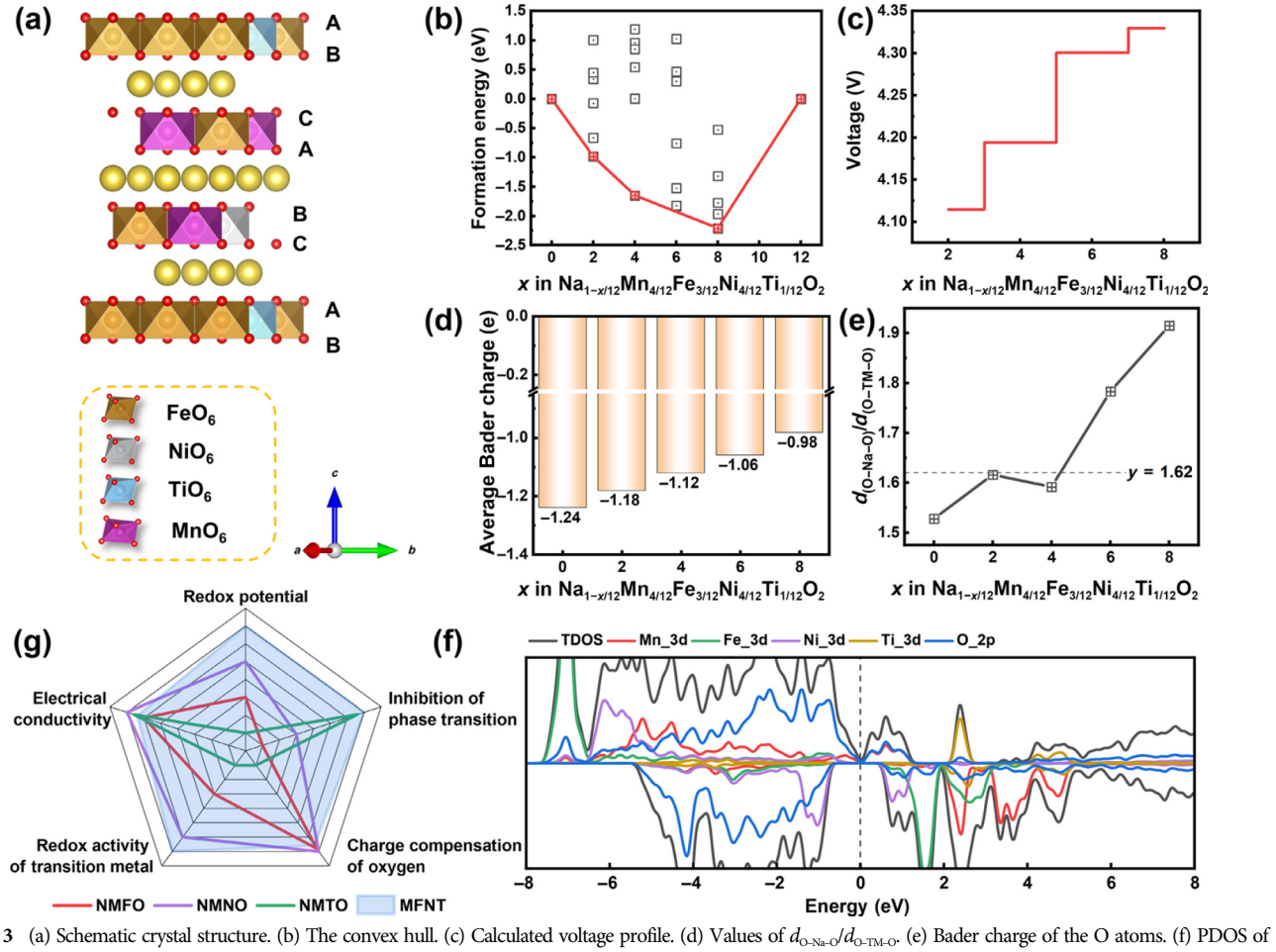

Figure 3 (a) Schematic crystal structure. (b) The convex hull. (c) Calculated voltage profile. (d) Values of $d_{O\text{-}Na\text{-}O}/d_{O\text{-}TM\text{-}O}$. (e) Bader charge of the O atoms. (f) PDOS of MFNT. (g) Property comparison of NMFO, NMNO, NMTO, and MFNT based on calculations.

gradual by the relatively high configurational entropy (1.286 R) of MFNT, as illustrated in Fig. S6 in the ESM, and the calculation is detailed in Eq. (S3) in the ESM [25]. As shown in Fig. 3(f), the PDOS of MFNT at the Fermi level are comparable to that of $NaMn_{8/12}Fe_{4/12}O_2$ (NMFO). This implies that, similar to NMFO, MFNT is influenced by the incorporation of Fe and fails to significantly improve the material's electrical conductivity. The property comparison between all singly doped compositions and MFNT is illustrated in Fig. 3(g). The comprehensive performance of MFNT has been significantly improved, implying that the utilization of first-principles calculations for designing medium-entropy cathodes with superior performance is anticipated to offer substantial benefits to the development of cathode materials.

2.2 Experimental verification

All samples were synthesized via a greener sol–gel route that minimizes volatile organic solvents and reduces energy consumption compared with conventional co-precipitation methods. In order to verify the variances in performance between MFNT and single-doped configurations, a series of comprehensive characterisations and electrochemical tests were conducted. The X-ray diffraction (XRD) patterns of all samples are presented in Fig. 4(a), wherein the diffraction peaks of all structures are indexed to an O3-type layered structure (PDF #54-0887) associated with the $R\bar{3}m$ space group [26]. The morphology and structure of the materials were investigated by scanning electron microscopy (SEM) and transmission electron microscopy (TEM) analyses. Figures 4(b)–4(e) reveal that NMFO, NMNO, and NMTO consist of irregular particles of 3–5 μm, whereas MFNT particles are predominantly 1–3 μm. Low-magnification SEM images (Figs. S7(a)–S7(d) in the ESM) confirm uniform sample production over a wide area. The smaller particles shorten the solid-state Na^+ diffusion length and enlarge the electrode–electrolyte interfacial area, both of which are beneficial for Na^+ transport and the overall electrochemical performance. High-magnification images (Figs. S7(e)–S7(h) in the ESM) show smooth and layered morphologies,

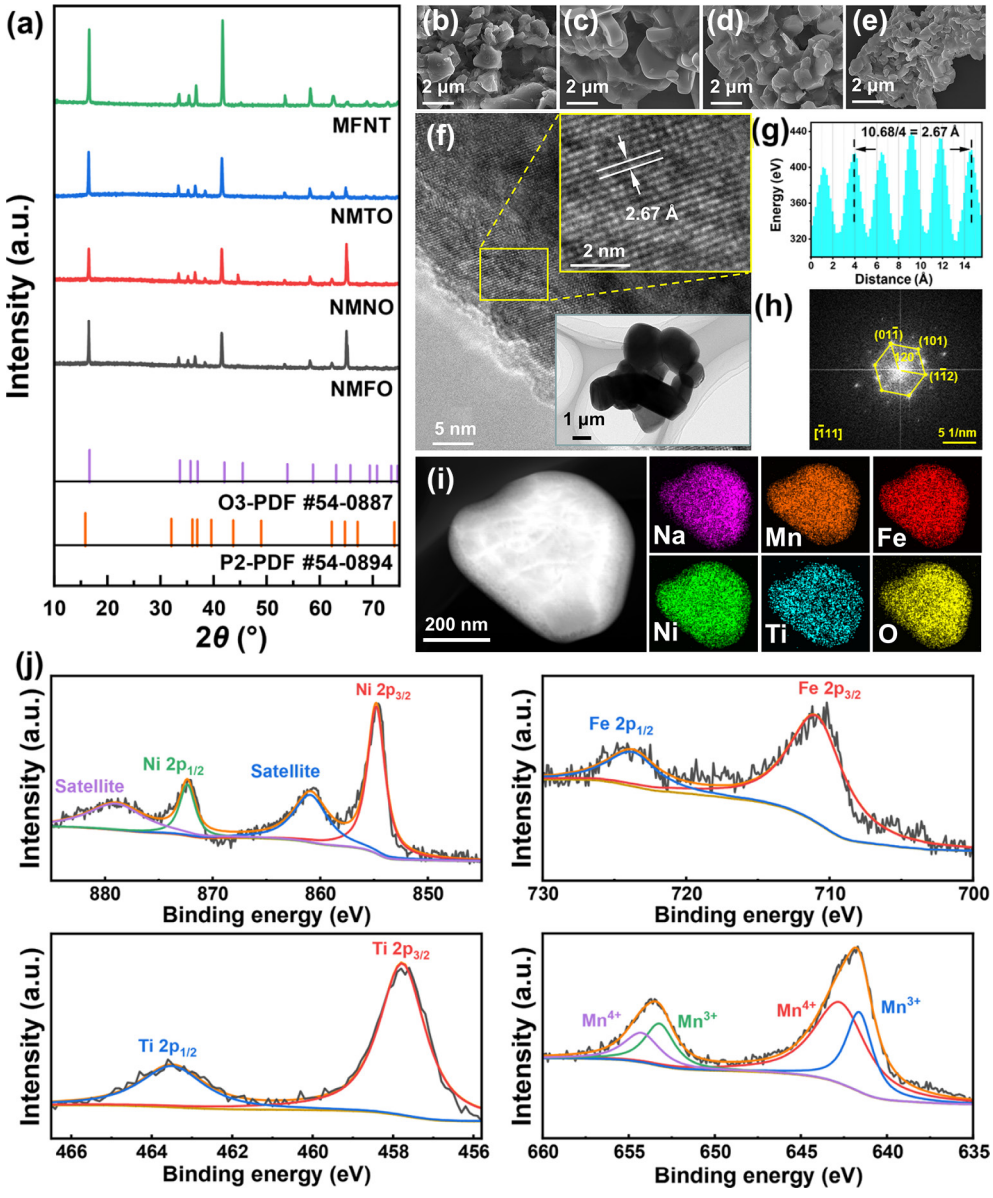

Figure 4 (a) XRD patterns of MFNT and doped materials. ((b)–(e)) SEM images of (b) NMFO, (c) NMNO, (d) NMTO, and (e) MFNT. (f) TEM image of MFNT, (g) corresponding line profiles of the Z-contrast information with the measured spacing, and (h) FFT pattern. (i) EDS mapping images of MFNT. (j) XPS spectra of MFNT.

indicative of high crystallinity, corroborated by high-resolution TEM (HRTEM, inset in Fig. 4(f) and Figs. S8(a)–S8(c) in the ESM). The corresponding line profiles of the Z-contrast information with the measured spacing are presented in Fig. 4(g). Lattice fringes with an interplanar spacing of 2.67 Å, corresponding to the (006) plane, are clearly resolved. The corresponding fast Fourier transformation (FFT) pattern depicted in Fig. 4(h), recorded along the [$\bar{1}$11] zone axis, confirms the single-crystal nature [27]. The uniform distribution of Na, Mn, Fe, Ni, Ti, and O elements within the MFNT framework is further confirmed through energy-dispersive X-ray spectrometry (EDS) mapping (Fig. 4(i) and Fig. S8(d) in the ESM).

XPS was employed to analyze the elemental composition and electronic states of the sample surface. The survey spectrum of MFNT (Fig. S9 in the ESM) exhibits characteristic peaks corresponding to Na 1s, Mn 2p, Fe 2p, Ni 2p, Ti 2p, and O 1s [5]. The Mn 2p spectrum (Fig. 4(j)) contains spin-orbit doublets at 641.6/653.2 eV (Mn^{3+}) and 642.8/654.2 eV (Mn^{4+}), confirming the coexistence of both oxidation states [28]. The Ni $2p_{3/2}$ (854.8 eV) and Ni $2p_{1/2}$ (872.3 eV) peaks, along with their satellite peaks at 861.0 and 879.2 eV in the Ni 2p spectrum, verify that Ni retains the +2 oxidation state [5]. The Fe $2p_{3/2}$ peak at 711.1 eV is assigned to Fe^{3+}, consistent with previous reports [26, 29]. In the Ti 2p spectra, the Ti $2p_{3/2}$ (457.8 eV) and Ti $2p_{1/2}$ (463.6 eV) peaks indicate that Ti exists as Ti^{4+} in the sample [5]. The oxidation states of all transition metals in doped configurations were verified by first-principles calculations. Before doping, the Mn sites possess a specific valence-electron count that facilitates diverse bonding interactions. Upon the introduction of foreign atoms, the local electronic environment of the Mn sites is modified, resulting in variations in their valence electron counts. According to the principle of charge conservation, the variation in the valence electron count of Mn^{3+} serves as a direct indicator of the electron transfer status of the dopant element within the chemical equilibrium configuration (TM^{3+} in $NaTMO_2$). The valence-electron difference of Mn^{3+} before and after doping is illustrated in Fig. S10(a) in the ESM. Mn7 in $NaMn_{11/12}Ni_{1/12}O_2$ undergoes a transition from Mn^{3+} to Mn^{4+} via electron loss, concomitant with the reduction of Ni^{3+} to Ni^{2+}. Similarly, Ti adopts the +4 oxidation state in $NaMn_{11/12}Ti_{1/12}O_2$. To elucidate bonding characteristics, electron localization function (ELF) maps on the (001) plane were calculated (Fig. S10(b) in the ESM). Compared with the pristine material, the variation observed in the charge density of Mn^{3+} within $NaMn_{11/12}Fe_{1/12}O_2$ is negligible. In the doped configurations involving Ni and Ti, the charge density of adjacent Mn^{3+} is found to be reduced and increased, respectively, suggesting an electron localization and delocalization phenomenon.

For electrochemical performance evaluation, the galvanostatic charge/discharge (GCD) curves of the materials are presented in Fig. 5(a) and Figs. S11(a)–S11(c) in the ESM, recorded at a current density of 0.1 C between 2.0 and 4.0 V. Reversible capacities of 120,

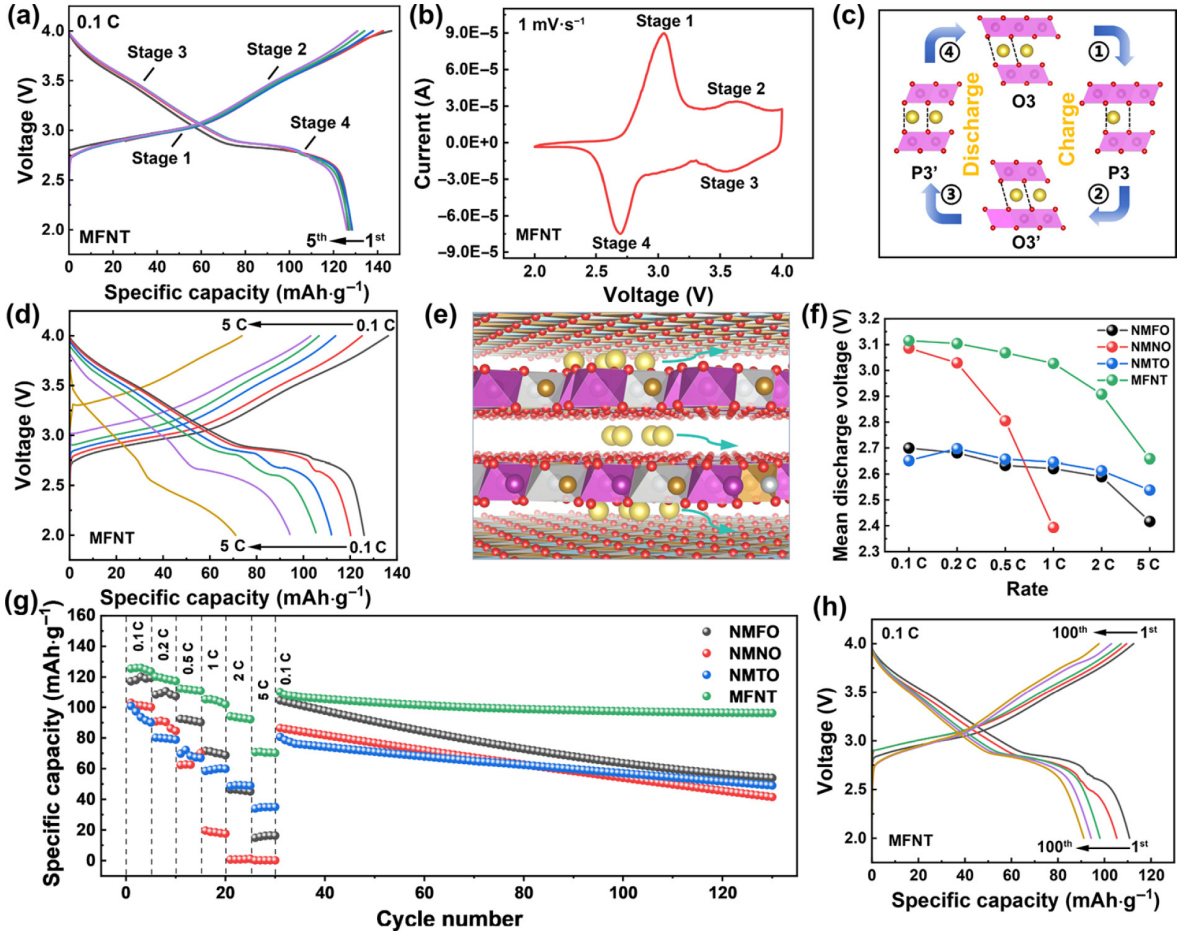

Figure 5 (a) GCD curves and (b) corresponding CV curves of MFNT. (c) Schematic diagram of phase transition during charging and discharging. (d) GCD curves at rates of 0.1, 0.2, 0.5, 1, 2, and 5 C. (e) The mean discharge voltages at different rates. (f) The schematic diagram of Na^+ migration in MFNT. (g) The rate capacity and cycling performance of NMFO, NMNO, NMTO, and MFNT. (h) GCD curves of initial 100 cycles for MFNT.

108, 108, and 127 mAh·g^{-1} were obtained for NMFO, NMNO, NMTO, and MFNT, respectively. The GCD curves of NMFO, NMNO, and NMTO exhibit several distinct voltage plateaus, indicating phase transitions (stages 1–6) that accompany TMO_2 slab gliding. In contrast, the MFNT curve is smoother and shows fewer plateaus (stages 1–4), implying that its medium-entropy crystalline structure undergoes fewer phase transitions. Cyclic voltammetry (CV) tests were performed at 0.1 mV·s^{-1} in Fig. 5(b) and Figs. S11(d)–S11(f) in the ESM, and the resulting CV curves exhibited good correspondence with the GCD analysis. Compared with the single-doped samples, the CV curve of MFNT demonstrates exceptional smoothness and presents the fewest redox peaks, highlighting its mild O3–P3 phase transitions (Fig. 5(c)). Rate performance was evaluated at various current densities and is shown in Fig. 5(d) and Fig. S12 in the ESM. MFNT delivers discharge capacities of 126, 120, 112, 105, 94, and 71 mAh·g^{-1} at 0.1, 0.2, 0.5, 1, 2, and 5 C, respectively. This indicates that the medium-entropy configuration of MFNT provides sufficient diffusion pathways for the rapid Na^+ migration, as illustrated in Fig. 5(e). Additionally, average discharge voltages at various rates are recorded in Fig. 5(f). The observed elevated average discharge voltage of MFNT indicates a higher energy density, consistent with the calculated results (Figs. 1(b) and 3(c)). In the post-rate cycling test (Fig. 5(g)), 96 mAh·g^{-1} is still retained by MFNT after 100 cycles, demonstrating substantial structural reversibility and capacity recovery. Moreover, compared with NMFO, NMNO, and NMTO, the characteristics of the long-term charge/discharge profiles of MFNT exhibit no significant variations during repeated (de)sodiation processes, underscoring its resilient structural integrity arising from entropy-stabilization effects (Fig. 5(h) and Fig. S13 in the ESM).

Further investigation and comparison of the apparent Na^+ migration kinetics are crucial for understanding the behavioral differences. Three evaluation methods were employed, one of which was based on CV curves recorded at sweep rates of 0.1–0.5 mV·s^{-1} (Fig. 6(a) and Figs. S14(a)–S14(c) in the ESM). Due to the enhanced polarization, the intensities and potential separations of all redox peaks increase with increasing scan rate. A linear relationship was obtained by plotting the peak current (i_p) against the square root of the scan rates ($v^{1/2}$), as shown in Fig. 6(b) and Figs. S14(d)–S14(f) in the ESM. The equations are given in Eqs. (S4)–(S6) in the ESM. The b values for the MFNT electrode, derived from peaks O2 and R2, are 1.019 and 0.803, respectively, indicating that sodium storage is predominantly capacitive. In contrast, the b values for O1 and R1 are 0.446 and 0.407, respectively, demonstrating that sodium storage in these peaks is dominated by Faradaic intercalation. The capacitive contribution percentages at various sweep rates were further calculated. As depicted in Fig. 6(c), a capacitive contribution of 66% is observed for MFNT at 0.1 mV·s^{-1}. Furthermore, Fig. 6(d) shows that the corresponding ratio values increase to 72%, 78%, 84%, and 91% at 0.2, 0.3, 0.4, and 0.5 mV·s^{-1}, respectively, confirming enhanced capacitive behavior at higher scan rates. Notably, the capacitance contributions of MFNT surpass those of singly doped samples across the entire scan-rate range (Fig. S15 in the ESM). These findings imply that the enhanced sodium-ion storage capacity of MFNT can be attributed to the higher proportion of capacitive contribution stemming from its medium-entropy structure.

As the second method, the galvanostatic intermittent titration technique (GITT) was additionally employed, as illustrated in Fig. 6(e) and Figs. S16(a)–S16(c) in the ESM. The diffusion coefficient of Na^+ (D_{Na^+}) was calculated by Eq. (S6) in the ESM. As depicted in Fig. 6(f) and Figs. S16(d)–S16(f) in the ESM, smaller fluctuations in D_{Na^+} values are exhibited by MFNT, with these values falling within a relatively narrow range of approximately 10^{-9}–10^{-10} cm^2·s^{-1}, outperforming those of NMFO, NMNO, and NMTO. Finally, *in-situ* electrochemical impedance spectroscopy (EIS) was implemented to probe the dynamic behavior (Fig. 6(g) and Figs. S17(a)–S17(c) in the ESM). The distribution of relaxation time (DRT) was employed to analyse the complex impedance responses and identify the multi-time-scale mechanisms involved in interfacial impedance evolution. Quantitative tracking of the variations in resistance associated with limitations in charge-transfer and mass-transport across the electrode–electrolyte interface is demonstrated in Fig. 6(h) and Figs. S17(d)–S17(f) in the ESM. As depicted in Fig. 6(i) and Figs. S17(g)–S17(i) in the ESM, spatiotemporal visualization of these processes is achieved via two-dimensional DRT contour plots, where three distinct relaxation-time peaks are observed. Peak 1 (P1) is attributed to the interfacial contact resistance between active material particles and the current collector, representing the efficiency of electron transport throughout the electrode matrix. Peak 2 (P2) is associated with the charge-transfer impedance inherent to the electrode material, serving as a quantification of the electrochemical reaction kinetics at the active material/electrolyte interface. Peak 3 (P3) displays temporal evolution characteristics that are tentatively linked to the dynamic restructuring of the cathode–electrolyte interphase (CEI) layer. The result demonstrates that the Na^+ diffusion resistance of MFNT primarily originates from the P2 and P3 stages, namely the charge-transfer process within the material and the reconstruction process of the CEI on the electrode surface. Initially, MFNT displays a relatively high electrochemical impedance of approximately 500 Ω during charging. As the voltage increases, this value declines rapidly to 30 Ω, confirming its exceptional ion-diffusion kinetics under high-voltage conditions. Subsequently, an increase in electrochemical impedance is observed during the discharge process. The entire charge–discharge cycle is characterised by high symmetry, which is the underlying cause of its exceptional cycling performance. The second-cycle EIS results (Fig. S18(a) in the ESM) demonstrate that the interfacial impedance decreases to below 400 Ω in the early charging stage, while the P3 segment (Fig. S18(c) in the ESM) exhibits enhanced symmetry. These observations indicate the formation of a stable CEI at the electrode–electrolyte interface following two charge–discharge cycles.

To gain deeper insight into the reaction mechanism and the crystal structure evolution, *ex-situ* XRD analysis was conducted during the first cycle (Fig. 6(j)). During the initial desodiation up to 2.5 V, the O3 structure remains stable without phase transition. Upon further Na^+ extraction, the (003) peak of the O3 phase splits and new peaks characteristic of the hexagonal P3 phase appear at lower angles, indicating a two-phase O3/P3 coexistence consistent with the 2.5–3.0 V plateau in the electrochemical profile. Upon continued extraction to 4.0 V, the mixed phase disappears and a new O3 phase (O3′) is subsequently generated. This corresponds precisely to the oxidation peak observed at 3.5 V in the CV curve (Fig. 5(b)). Upon discharge, when the voltage decreases to 3.5 V, the diffraction peak corresponding to the O3′ phase shifts leftward and subsequently splits into a new P3 phase (P3′). O3′ is a distorted O3-type layered phase generated by Na^+ ordering and lattice distortion during deep charging, while P3′ is a modified P3-type phase formed

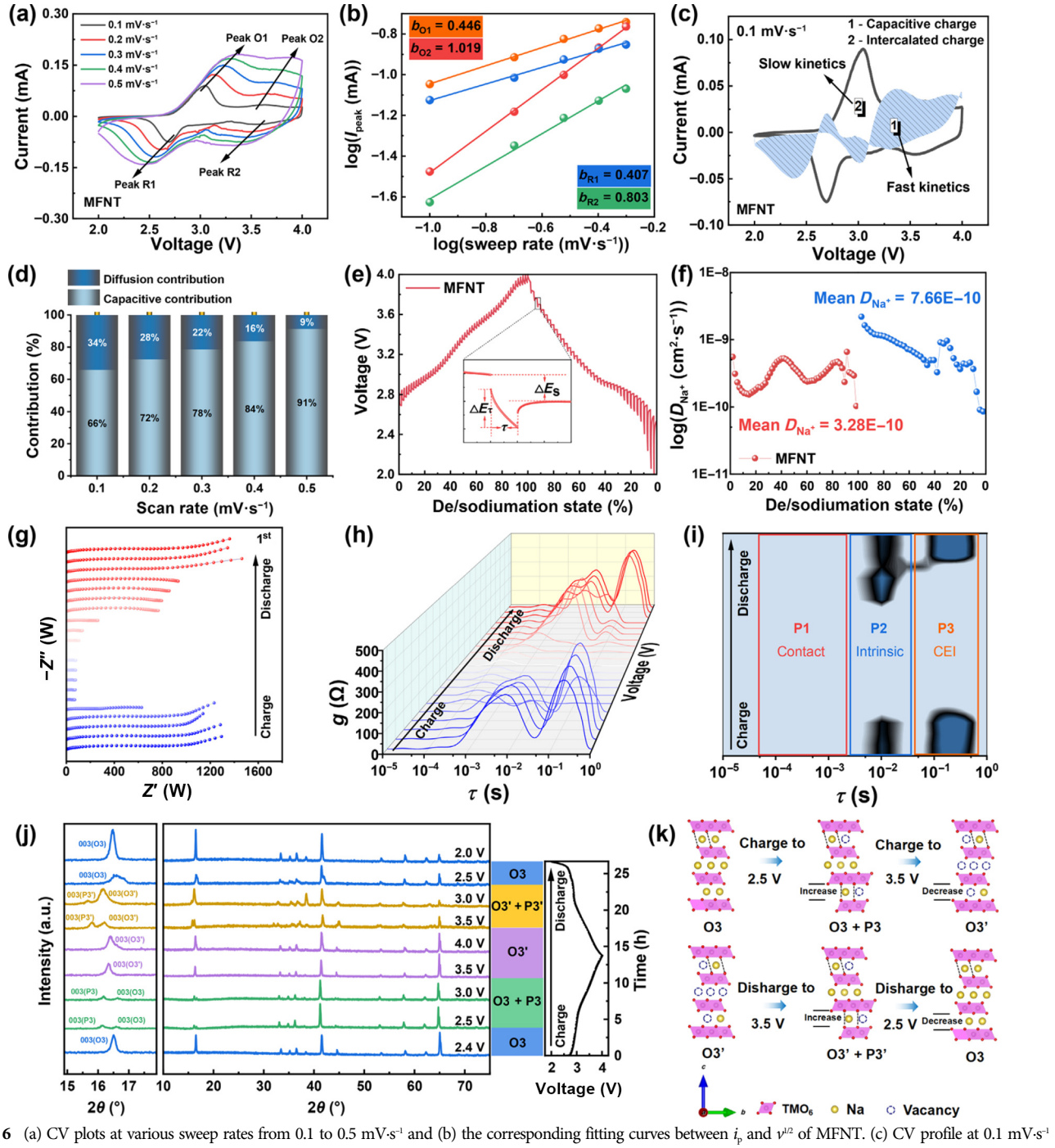

Figure 6 (a) CV plots at various sweep rates from 0.1 to 0.5 mV·s^{-1} and (b) the corresponding fitting curves between i_p and $v^{1/2}$ of MFNT. (c) CV profile at 0.1 mV·s^{-1} expressing the pseudocapacitive contribution (blue region) to the total current and (d) the corresponding capacity contribution ratio at different scan rates for MFNT. (e) GITT profiles in the initial charge/discharge process and (f) the corresponding calculated D_{Na+} values for MFNT. (g) *In-situ* EIS for MFNT. (h) DRT curves and (i) their contour maps for MFNT. (j) The *ex-situ* XRD pattern for the first charge/discharge process at the rate of 0.1 C in the voltage range between 2.0 and 4.0 V. (k) Schematic illustration of phase evolution during charging and discharging for MFNT.

by the rearrangement of transition metal slabs to adapt to partial Na^+ extraction. As desodiation proceeds, the structure completely recovers to the original state after a full cycle, indicating a reversible phase transition. The structural evolution during the entire charge–discharge process is depicted in Fig. 6(k). Upon removal of Na^+, the electrostatic repulsion between O atoms within the O–Na–O slabs intensifies because the shielding effect is lost. Consequently, the O–Na–O slabs expand while the O–TM–O slabs contract, driving the O3 → P3 phase transition. When Na^+ is further extracted up to 3.5 V, the O–Na–O layers collapse for lack of Na, causing the O–Na–O slabs to shrink and the O–TM–O slabs to expand. This ultimately triggers a further transition from the P3 phase to a new O3 phase (O3′). This ultimately results in the further phase transition from the P3 phase to a novel O3 phase (O3″). The phase transitions that occur during discharge are exactly reversed during charging. Comparative analysis reveals that the superior mild phase transition and high reversible capacity exhibited by MFNT are ascribed to its optimized medium-entropy configuration

(Fig. S19 in the ESM). The coexistence of these two phases reflects the structural adaptability of the cathode material under electrochemical cycling, which contributes to its excellent rate performance and cycling stability. Beyond sodium-ion batteries, this medium- and high-entropy design strategy exhibits equal universality for lithium-ion batteries, potassium-ion batteries, aqueous systems, and other entropy-stabilized electrode families.

3 Conclusions

A medium-entropy (1.286 R) O3-type cathode MFNT was quantitatively designed by first-principles calculations and successfully synthesized. Theoretical screening assigns Ni, Fe, and Ti to boost potential, stabilize Fe^{3+}/Fe^{4+}, and suppress Jahn–Teller distortion, yielding an optimal dopant dosage that balances overall performance. Experimental validation confirmed that the entropy-stabilized structure delivered 127 $mAh{\cdot}g^{-1}$ at 0.1 C, retained 96 $mAh{\cdot}g^{-1}$ after 100 cycles, and sustained 71 $mAh{\cdot}g^{-1}$ at 5 C. The reversible oxygen redox process is evidenced by the Bader charge transition of oxygen from –1.24 e to –0.98 e, through which additional capacity is obtained without relying on expensive or toxic transition metals. Capacitive-dominated Na^+ storage behavior and stable diffusion coefficients are revealed by CV, GITT, and *in-situ* EIS analyses. The reversible phase transitions of O3 → (O3 + P3) → O3′ → (O3′ + P3′) → O3 in MFNT featuring a mediumentropy configuration were further corroborated by *ex-situ* XRD. Overall, the integrated computational–experimental approach demonstrated in this study not only markedly shortens the development cycle of sodium-ion battery cathodes but also exhibits universal applicability to lithium-ion, zinc-ion, and other battery chemistries.

Electronic Supplementary Material: Supplementary material (crystal structure, Bader charge, DOS, configurational entropy, SEM images, TEM images, ELF, electrochemical performance, and XPS spectra) is available in the online version of this article at https://doi.org/10.26599/NR.2026.94908572.

Data availability

All data needed to support the conclusions in the paper are presented in the manuscript and the Electronic Supplementary Material. Additional data related to this paper may be requested from the corresponding author upon request.

Acknowledgements

This work was financially supported by the Key Scientific and Technological Project of Henan Province (No. 242102240078) and the Ph.D. Research Start-up Fund of Anyang Institute of Technology (No. BSJ2021009).

Declaration of competing interest

All the contributing authors report no conflict of interests in this work.

Author contribution statement

C. Z.: Data curation, writing manuscript. N. F. and H. H. Z.: Funding acquisition. W. L. J.: Experimental design. J. C. F., B. W. Z., P. T. W., K. X., and L. L.: Project administration, supervision. All the authors have approved the final manuscript.

Use of AI statement

None.

References

[1] Wang, X.; Yin, X. P.; Feng, X. C.; Li, Y.; Dong, X. P.; Shi, Q. H.; Zhao, Y. F.; Zhang, J. J. Rational design of $Na_{0.67}Ni_{0.2}Co_{0.2}Mn_{0.6}O_2$ microsphere cathode material for stable and low temperature sodium ion storage. *Chem. Eng. J.* **2022**, *428*, 130990.

[2] Guo, Z. Q.; Li, X. R.; Lyu, Y. C.; Xu, S. Y. Improved electrochemical performance of B doped O'3-$NaMnO_2$ for Na-ion battery. *Electrochim. Acta* **2022**, *430*, 141079.

[3] Zhou, D.; Ning, D.; Wang, J.; Liu, J. H.; Zhang, G. Y.; Xiao, Y. G.; Zheng, J. X.; Li, Y. L.; Li, J.; Liu, X. Z. Clarification of underneath capacity loss for O3-type Ni, Co free layered cathodes at high voltage for sodium ion batteries. *J. Energy Chem.* **2023**, *77*, 479–486.

[4] Hong, N. Y.; Li, J. W.; Guo, S. H.; Han, H. W.; Wang, H. J.; Hu, X. Y.; Huang, J. N.; Zhang, B. C.; Hua, F.; Song, B. et al. An *in situ* dual-modification strategy for O3-$NaNi_{1/3}Fe_{1/3}Mn_{1/3}O_2$ towards high-performance sodium-ion batteries. *J. Mater. Chem. A* **2023**, *11*, 18872–18880.

[5] Wang, H.; Liu, Q. M.; Liu, Y. R. Multi-ion doped P2/O3 biphasic layered oxides cathodes $Na_xNi_{0.2}Mn_{0.55}Cu_{0.14}Ti_yZn_zO_2$ for sodium-ion batteries. *J. Alloys Compd.* **2023**, *962*, 171053.

[6] Hong, F. F.; Zhou, X.; Liu, H.; Feng, G. L.; Liu, X. H.; Zhang, H.; Fan, W. F.; Zhang, B.; Zuo, M. H.; Xing, W. Y. et al. Medium-entropy configuration enabling reversible P2-OP4 phase transition in layered oxides for high-rate sodium-ion batteries. *Rare Met.* **2025**, *44*, 2997–3007.

[7] Liu, Q. N.; Hu, Z.; Chen, M. Z.; Zou, C.; Jin, H. L.; Wang, S.; Chou, S. L.; Dou, S. X. Recent progress of layered transition metal oxide cathodes for sodium-ion batteries. *Small* **2019**, *15*, 1805381.

[8] Zhong, X. B.; He, C.; Gao, F.; Tian, Z. Q.; Li, J. F. *In situ* Raman spectroscopy reveals the mechanism of titanium substitution in P2-$Na_{2/3}Ni_{1/3}Mn_{2/3}O_2$: Cathode materials for sodium batteries. *J. Energy Chem.* **2021**, *53*, 323–328.

[9] Liu, H. Q.; Gao, X.; Chen, J.; Gao, J. Q.; Yin, S. Y.; Zhang, S.; Yang, L.; Fang, S. S.; Mei, Y.; Xiao, X. H. et al. Reversible OP4 phase in P2-$Na_{2/3}Ni_{1/3}Mn_{2/3}O_2$ sodium ion cathode. *J. Power Sources* **2021**, *508*, 230324.

[10] Xiao, Y.; Zhu, Y. F.; Yao, H. R.; Wang, P. F.; Zhang, X. D.; Li, H. L.; Yang, X. N.; Gu, L.; Li, Y. C.; Wang, T. et al. A stable layered oxide cathode material for high-performance sodium-ion battery. *Adv. Energy Mater.* **2019**, *9*, 1803978.

[11] Gao, X.; Chen, J.; Liu, H. Q.; Yin, S. Y.; Tian, Y.; Cao, X. Y.; Zou, G. Q.; Hou, H. S.; Wei, W. F.; Chen, L. B. et al. Copper-substituted Na_xMO_2 (M = Fe, Mn) cathodes for sodium ion batteries: Enhanced cycling stability through suppression of Mn(III) formation. *Chem. Eng. J.* **2021**, *406*, 126830.

[12] Ge, Q. L.; Fan, L. Z.; Ai, Q.; Na, M.; Ding, X. L. Atoms regulation O3-type $NaNi_{0.3}Fe_{0.4}Mn_{0.3}O_2$ as cathodes for enhanced electrochemical performance sodium-ion batteries. *Ionics* **2025**, *31*, 12963–12973.

[13] Yang, T. T.; Huang, Y. L.; Zhang, J.; Zhu, H.; Ren, J. C.; Li, T. Y.; Gallington, L. C.; Lan, S.; Yang, L. G.; Liu, Q. Insights into Ti doping for stabilizing the $Na_{2/3}Fe_{1/3}Mn_{2/3}O_2$ cathode in sodium ion battery. *J. Energy Chem.* **2022**, *73*, 542–548.

[14] Lee, I.; Oh, G.; Lee, S.; Yu, T. Y.; Alfaruqi, M. H.; Mathew, V.; Sambandam, B.; Sun, Y. K.; Hwang, J. Y.; Kim, J. Cationic and transition metal co-substitution strategy of O3-type $NaCrO_2$ cathode for high-energy sodium-ion batteries. *Energy Storage Mater.* **2021**, *41*, 183–195.

[15] Zhang, C.; Zhao, H. H.; Wang, P. T.; Xie, K.; Wang, C. Y.; Zhang, B. W.; Jia, W. L.; Fu, N.; Lin, L. Inhibition of phase transition in sodium-ion battery cathode material: From design to validation. *J. Alloys Compd.* **2025**, *1036*, 181798.

[16] Duan, L. P.; Zhang, Y. N.; Tang, H. W.; Liao, J. Y.; Zhou, G. M.; Zhou, X. S. Recent advances in high-entropy layered oxide cathode materials for alkali metal-ion batteries. *Adv. Mater.* **2025**, *37*, 2411426.

[17] Ren, Y.; Ge, Q. L.; Wu, Y. J.; Peng, Q.; Qian, J.; Ding, X. L. A high-entropy cathode for sodium-ion batteries: Cu/Zn-doping O3-type Ni/Fe/Mn layer oxides. *J. Phys. Chem. Solids* **2024**, *194*, 112241.

[18] Yao, L. B.; Zou, P. C.; Wang, C. Y.; Jiang, J. H.; Ma, L.; Tan, S.; Beyer, K. A.; Xu, F.; Hu, E. Y.; Xin, H. L. High-entropy and superstructure-stabilized layered oxide cathodes for sodium-ion batteries. *Adv. Energy Mater.* **2022**, *12*, 2201989.

[19] Mu, J. X.; Cai, T. X.; Dong, W. J.; Zhou, C.; Han, Z.; Huang, F. Q. Biphasic high-entropy layered oxide as a stable and high-rate cathode for sodium-ion batteries. *Chem. Eng. J.* **2023**, *471*, 144403.

[20] Sun, C.; Ni, Q.; Li, M.; Sun, Z.; Yuan, X. Y.; Li, L.; Wang, K. Y.; Jin, H. B.; Zhao, Y. J. Improving rate performance by inhibiting Jahn–Teller effect in Mn-based phosphate cathode for Na-ion Batteries. *Adv. Funct. Mater.* **2023**, *34*, 2310248.

[21] Zhao, C. L.; Avdeev, M.; Chen, L. Q.; Hu, Y. S. An O3-type oxide with low sodium content as the phase-transition-free anode for sodium-ion batteries. *Angew. Chem., Int. Ed.* **2018**, *57*, 7056–7060.

[22] Zhao, C. L.; Wang, Q. D.; Yao, Z. P.; Wang, J. L.; Sanchez-Lengeling, B.; Ding, F. X.; Qi, X. G.; Lu, Y. X.; Bai, X. D.; Li, B. H. et al. Rational design of layered oxide materials for sodium-ion batteries. *Science* **2020**, *370*, 708–711.

[23] Gao, X. Y.; Lian, R. Q.; He, L.; Fu, Q.; Indris, S.; Schwarz, B.; Wang, X. D.; Chen, G.; Ehrenberg, H.; Wei, Y. J. Phase transformation, charge transfer, and ionic diffusion of $Na_4MnV(PO_4)_3$ in sodium-ion batteries: A combined first-principles and experimental study. *J. Mater. Chem. A* **2020**, *8*, 17477–17486.

[24] Luo, Y. F.; Shen, J. L.; Yao, Y.; Dai, J. Y.; Ling, F. X.; Li, L.; Jiang, Y.; Wu, X. J.; Rui, X. H.; Yu, Y. Inhibiting the Jahn–Teller effect of manganese hexacyanoferrate via Ni and Cu codoping for advanced sodium-ion batteries. *Adv. Mater.* **2024**, *36*, 2405458.

[25] Zhao, Q.; Lin, Y. X.; Avdeev, M.; Ren, Y. R.; Shi, L.; Xu, S. K.; Shi, S. Q. Beyond order: Partial site occupancies-informed machine learning for solid-state electrolytes design. *Chem. Mater.* **2025**, *37*, 10006–10013.

[26] Xu, S. W.; Chen, H. X.; Li, C.; Nie, R. H.; Yang, Y. T.; Zhou, M. C.; Zhang, X. Y.; Zhou, H. M. Effect of Ti doping on the structural and electrochemical performance of O3-type $Na(Ni_{0.3}Fe_{0.2}Mn_{0.5})_{1-x}Ti_xO_2$ cathode materials for sodium-ion batteries. *J. Alloys Compd.* **2023**, *962*, 171199.

[27] Zhao, S. Y.; Shi, Q. H.; Feng, W. L.; Liu, Y.; Yang, X. X.; Zou, X. L.; Lu, X. G.; Zhao, Y. F. Suppression of multistep phase transitions of O3-type cathode for sodium-ion batteries. *Chin. Chem. Lett.* **2024**, *35*, 108606.

[28] Rui, L.; Feng, W.; Man, X.; Yao, Y.; Zhou, J. H.; Huang, Y. X.; Ye, Y. S.; Li, L.; Chen, R. J. Habit plane-driven P2-type manganese-based layered oxide as long cycling cathode for Na-ion batteries. *J. Power Sources* **2018**, *383*, 80–86.

[29] Yuan, D. D.; Wang, Y. X.; Cao, Y. L.; Ai, X. P.; Yang, H. X. Improved electrochemical performance of Fe-substituted $NaNi_{0.5}Mn_{0.5}O_2$ cathode materials for sodium-ion batteries. *ACS Appl. Mater. Interfaces* **2015**, *7*, 8585–8591.